












Research Article

Preparation and Characterization of Patuletin-Loaded Chitosan Nanoparticles with Improved Selectivity and Safety Profiles for Anticancer Applications

Ahmed M. Metwaly ^{1,2}, Ahmed M. Abdel-Raouf ³, Abdulaziz M. Alattar ³,
Adham A. El-Zomrawy ⁴, Ashraf M. Ashmawy ⁴, Metwally G. Metwally ⁵,
Mohamed A. Abu-Saied ⁶, Asmaa M. Lotfy ⁶, Bshra A. Alsouk ⁷, Eslam B. Elkaeed ⁸,
and Ibrahim H. Eissa ⁹

¹Pharmacognosy and Medicinal Plants Department, Faculty of Pharmacy (Boys), Al-Azhar University, Cairo 11884, Egypt

²Biopharmaceutical Products Research Department, Genetic Engineering and Biotechnology Research Institute, City of Scientific Research and Technological Applications (SRTA-City), Alexandria, Egypt

³Analytical Chemistry, Department of Pharmaceutical Analytical Chemistry Faculty of Pharmacy, Al-Azhar University, Nasr City, Cairo, Egypt

⁴Chemistry Department, Faculty of Science (boys), Al-Azhar University, Cairo 11884, Egypt

⁵Zoology Department, Faculty of Science (Boys), Al-Azhar University, Cairo 11884, Egypt

⁶Polymeric Materials Research Department, Advanced Technology and New Materials Research Institute, City of Scientific Research and Technological Applications (SRTA-CITY), New Borg El-Arab City 21934, Alexandria, Egypt

⁷Department of Pharmaceutical Sciences, College of Pharmacy, Princess Nourah bint Abdulrahman University, P.O. Box 84428, Riyadh 11671, Saudi Arabia

⁸Department of Pharmaceutical Sciences, College of Pharmacy, AlMaarefa University, Riyadh 13713, Saudi Arabia

⁹Pharmaceutical Medicinal Chemistry & Drug Design Department, Faculty of Pharmacy (Boys), Al-Azhar University, Cairo 11884, Egypt

Correspondence should be addressed to Ahmed M. Metwaly; ametwaly@azhar.edu.eg and Ibrahim H. Eissa; ibrahimeissa@azhar.edu.eg

Received 21 February 2023; Revised 26 June 2023; Accepted 11 July 2023; Published 24 July 2023

Academic Editor: Luis F. Guido

Copyright © 2023 Ahmed M. Metwaly et al. This is an open access article distributed under the Creative Commons Attribution License, which permits unrestricted use, distribution, and reproduction in any medium, provided the original work is properly cited.

Objective. This study aimed to investigate the preparation of patuletin-encapsulated chitosan nanoparticles (PT-CS-NPs) using the ionic gelation method, evaluate their potential as anticancer agents, and invent a new method of differential pulse voltammetric analysis for patuletin (PT). **Methods.** Computational studies were conducted to assess the affinity of PT for chitosan, confirming a promising interaction. PT-CS-NPs were synthesized based on the computational outputs, resulting in nanoparticles with an angular structure and an average size of 6.168 nm. The cytotoxicity of PT and PT-CS-NP was evaluated in breast and colon cancer cell lines, and selectivity indices were calculated to assess safety profiles. The electrochemical behavior of PT was also investigated using the Britton–Robinson buffer. **Results.** PT-CS-NP exhibited both potent cytotoxicity and a favorable safety profile, showing the most active and safest pattern of cytotoxicity among the tested compounds. The electrochemical oxidation of PT was observed at 0.531 V vs. Ag/AgCl at pH 4.0. The concentration of PT showed a linear relationship with the corresponding peak current over the range of (10.0×10^{-9} : 10.0×10^{-5} M) M, with a minimum limit of detection of 3.4×10^{-9} M. The proposed method successfully measured PT, with a relative standard deviation below 2%. **Conclusion.** The preparation of PT-CS-NP via the ionic gelation method resulted in angular nanoparticles with a promising anticancer activity and safety profiles. The electrochemical behavior of PT was characterized, and a reliable method for PT quantification was established.

1. Introduction

Globally, cancer is the 2nd major death cause after cardiovascular diseases, according to the reports that have been published by the World Health Organization (WHO). More seriously, cancer is expected to become the major cause of death within the next few years. As per the World Health Organization's report, breast cancer exhibited a predominant incidence rate concerning the number of newly diagnosed cases, surpassing 2.2 million globally in the year 2020 [1]. Colorectal cancer is the third most common cancer in men and the second most common in women, with around 2 million new cases reported in 2020. However, it also ranks second in cancer-related deaths, causing approximately one million fatalities worldwide, according to the International Agency for Research on Cancer (IARC) [2].

The use of natural resources for medicinal purposes is a practice that dates back to early civilizations such as the ancient Egyptian and Chinese medicines [3–5]. The reliance on nature for fulfilling human needs is deeply ingrained in our history and continues to play a vital role in our lives today.

Patuletin (PT, Figure 1) is a rare trimethoxyflavone that was identified from *Tagetes patula* for the first time in 1941 [6]; then, it has been isolated from other plant species such as *Urtica urens* [7] and *Eriocaulon* sp. [8]. Later, it was used as a marker for the flowers of *Tagetes patula* [9]. Although being rare, PT's cytotoxicity was reported in several records. It exhibited cytotoxicity employing the Allium test with an IC₅₀ value of ~100 µg/mL [10]. Also, at a concentration of 1 µM, PT reduced the helenalin-induced cytotoxicity by a percentage of 40% [11]. Similarly, PT induced necrosis and apoptosis in CaSki (cervical), MDA-MB-231 (breast), and SK-Lu-1 (lung) cancer cell lines [12]. In another study, PT expressed high cell growth inhibition (GI₅₀: 0.6 ± 0.1 µg/ml) and cytotoxicity (LC₅₀: 2.5 ± 0.1 µg/ml) against the HeLa cancer cell line [13]. In addition, PT inhibited the growth of GLC4 and COLO 320 cancer cell lines with IC₅₀ values of 160 and 147 µM, respectively [14]. Furthermore, various promising bioactivities of PT such as anti-inflammatory [15, 16], antimicrobial [17, 18], and neuroprotective [19] were reported.

A new drug delivery technology is revolutionizing drug discovery creating a pharmaceutical industry focused on research and development [20–22]. Chitosan is a natural polymer from marine crustaceans biosynthesized by *n*-deacetylation that shows biocompatible, biodegradable, and high drug loading efficiency when used as a nanoparticle polymer [23–26]. Differential pulse voltammetric analysis is an electrochemical method employed to detect and quantify diverse analytes. It encompasses applying a sequence of potential pulses to the working electrode and measuring the resulting current. This technique provides notable sensitivity, selectivity, and versatility, finding applications in pharmaceutical analysis, environmental monitoring, and food safety assessment, among other fields [27].

We herein report the development of a novel preparation of PT-encapsulated chitosan nanoparticles as a nanocarrier

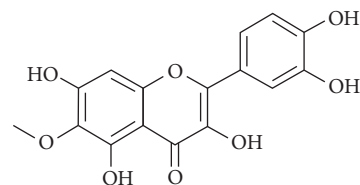


FIGURE 1: Chemical structure of PT.

model in order to improve the anticancer activities against breast and colon cancer. Furthermore, we present a novel differential pulse voltammetric analysis method for PT.

2. Results and Discussion

2.1. In Silico Studies. At first, molecular docking experiments were performed to examine the possible binding pattern and orientation of PT into chitosan. The calculated ΔG (binding free energy) of PT was -53.03 Kcal/mol. The negative free energy indicated the spontaneous binding mode.

The binding mode of PT inside the chitosan molecule is clarified in Figures 2 and 3. PT formed one hydrogen bond and two hydrophobic interactions. The hydroxyl group at the 3rd position of the phenyl ring formed a hydrogen bond. At the same time, the phenyl and the 4H-chromen-4-one moieties were incorporated in two hydrophobic interactions with the alkyl moieties of chitosan.

The *in silico* molecular docking experiment could revolve around the potential use of chitosan as a carrier for PT and determined binding patterns and orientations. The negative binding free energy (ΔG) value obtained in this study indicated the spontaneous binding mode. The hydrogen bond and hydrophobic interactions formed between PT and chitosan provide insight into the specific mechanisms of their binding interactions. This information could be used to design and develop new drug delivery systems, utilizing the natural properties of chitosan and the molecular properties of PT. The use of molecular docking experiments provided a useful tool for understanding the binding patterns and mechanisms of drug-carrier interactions, which could have important implications for the development of new drug delivery systems.

2.2. Preparation of PT-CS-NP

2.2.1. Synthesis of PT-CS-NP. The used PT in this study was isolated by our team before [28]. Chitosan nanoparticles were synthesized by a method called ionotropic gelation, depending on the ionic interaction between negatively charged TPP and positively charged chitosan (CS) as reported before [29]. The method is described in detail in the method part of the supplementary data.

2.2.2. FTIR Spectral Analysis. The FTIR spectra of CS/TPP and patuletin-loaded CS/TPP nanoparticles (PT-CS-NPs) are shown in Figure 4. In CS nanoparticles, the strong and wide peaks in the 3409 and 3277 cm^{-1} correspond to N-H and O-H stretching, respectively [30]. The absorption bands

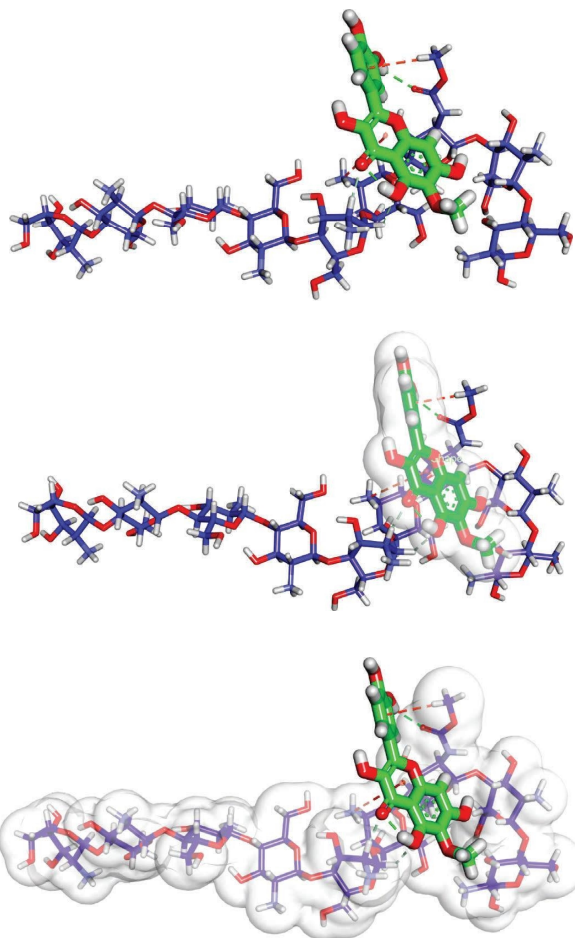


FIGURE 2: Top view of the binding mode of PT (green) inside chitosan (blue) forming a hydrogen bond and two hydrophobic interactions.

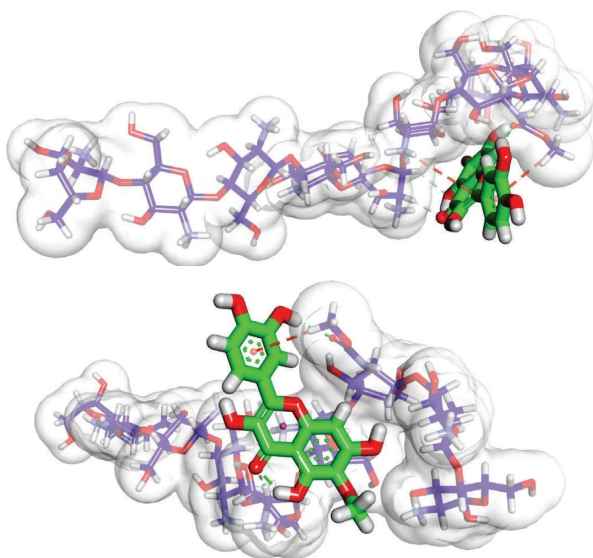


FIGURE 3: Side view of the binding mode of PT (green) inside chitosan (blue) forming one hydrogen bond and two hydrophobic interactions.

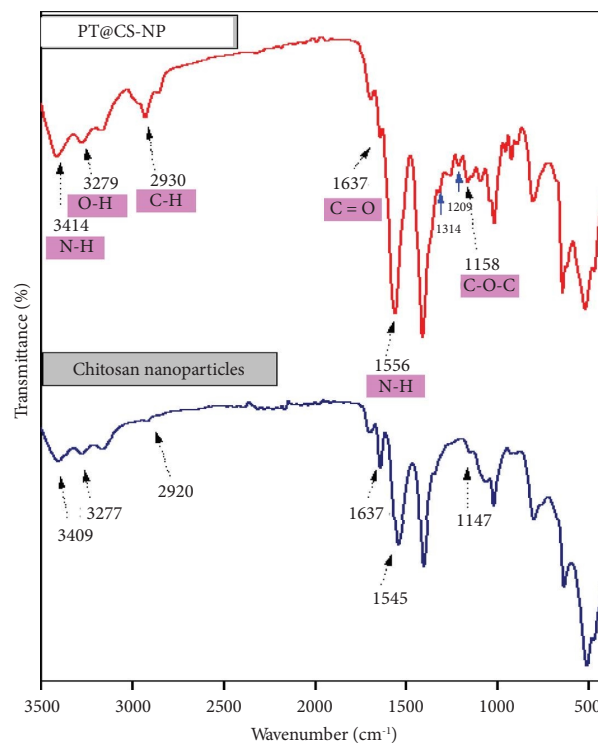


FIGURE 4: FT-IR of CS and PT-CS-NP.

at 2920 cm^{-1} can be attributed to C-H stretching. The existence of bands at 1637 cm^{-1} belongs to amide I C=O stretching. The N-H bending of the main amine is shown by a band at 1545 cm^{-1} . The asymmetric stretching of the C-O-C bridge is responsible for the absorption band at 1147 cm^{-1} [31, 32]. The presence of TPP was further verified in the NPs' spectra by the two strong absorption bands. Peaks in the region of $1220\text{--}1080\text{ cm}^{-1}$ can be attributed to the P-O stretch, and peaks in the range of 899 cm^{-1} –P-O combined with P-O-P. The displacement of these two bands, as well as the enhanced intensity of the NH_2 band, showed an ionic interaction between the positively charged amino groups of the CS and the negatively charged groups of the NH_2 of TPP [33, 34]. The FTIR spectra of PT-CS-NP show aromatic bonding at 1556 cm^{-1} , O-H phenol stretching at 3414 cm^{-1} , -C-C- ((in-ring) aromatic) band at 1556 cm^{-1} , C-O stretching of ethers linkage and -C-O- (polyols) appeared at 1314 and 1209 cm^{-1} , respectively, and -C-OH stretching at 1314 cm^{-1} . The presence of these peaks shows confirmation of PT-CS-NP.

2.2.3. Morphology. The typical morphology and the particle size of PT-CS-NP were investigated by scan electron microscopy (SEM) and transmission electron microscopy (TEM). As shown in Figure 5, SEM images show some agglomerated particles, which can be due to the softening process during the NP synthesis. The nanoparticles had a compact structure, a nearly spherical form, and a heterogeneous morphology, as seen by TEM pictures.

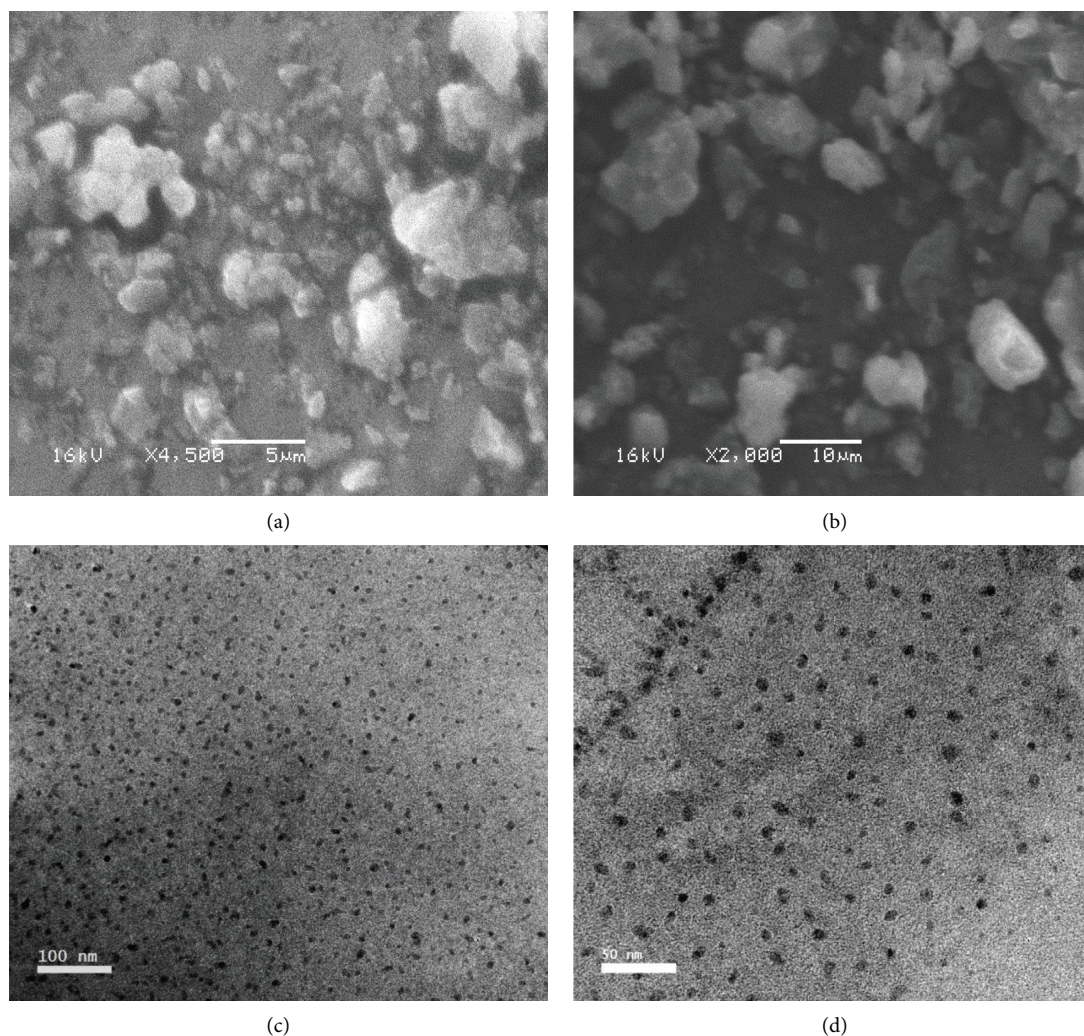


FIGURE 5: SEM images of PT-CS-NP: (a) 4500X and (b) 2000X. TEM images of PT-CS-NP at (c) 50 nm and (d) 100 nm.

Furthermore, a solid core surrounded by the polymer was found, which most likely did not interact throughout the NP formation [35, 36]; on the other hand, PT-CS-NP shows small particles due to the presence of PT with a more angular structure than spherical, and the size varies between 4 and 11 nm with average size = 6.168 nm that are suitable for drug delivery application.

2.2.4. Thermo Gravimetric Analysis (TGA). In Table 1 and Figure 6, TGA analysis shows typical three stages of weight loss for CS NPs; the resulting maximum loss was ~60%. The 1st stage at 60°C reflects water molecules' loss, which could be associated with the hydroxyl and amine groups of the resulting polymer, through hydrogen bonding. The 2nd stage is corresponding to the CS and TPP ionic bond destruction and disintegrated nanoparticles [37] at 272°C. The 3rd stage at 412°C may be related to the thermal degradation of the main polymer backbone [36, 38]. For PT-CS-NP, three stages of mass loss were also detected. The 1st stage is at 70°C due to water loss, and the 2nd stage is at 272°C resulting from

TABLE 1: TGA of CS NPs and PT-CS-NP.

Samples	Weight loss (%)					
	T10	T20	T30	T40	T50	T60
CS NPs	59.8	74.1	143.5	266.3867	305.1	430.7
PT-CS-NP	70.1	187.8	272.7	333.9	412.7	731.8

nanoparticle degradation. The maximum percentages of degradation observed in the TG curves of CS/TPP and PT-CS-NP were ~70 and ~60%, respectively.

However, it was observed that comparing CS/TPP NPs, the temperature degrees obtained for PT-CS-NP were lower, which corresponds to the presence of PT resulting in the reduction of the thermal stability values of chitosan. Furthermore, the total weight loss in CS/TPP NPs was higher than PT-CS-NP, indicating a higher thermal stability of the obtained nanoparticles. This may be due to the strong electrostatic interactions that occur between PT and both the phosphate and amino groups from TPP and chitosan.

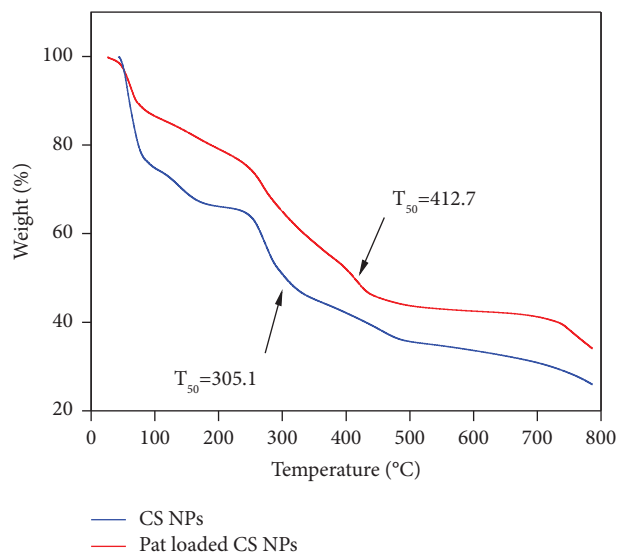


FIGURE 6: TGA curves of (a) CS NPs and (b) PT-CS-NP.

2.3. Biological Evaluation

2.3.1. In Vitro Anticancer Potentialities. *In vitro* cytotoxicity examination of the anticancer potentialities of CS, PT, and PT-CS-NP against breast cancer cell lines, MCF-7, and human colon cancer cell lines, HCT 116, was proceeded utilizing sorafenib as a reference. As shown in Table 2 and Figure 7, PT-CS-NP was the most active candidate inhibiting both cell lines with IC_{50} values of 2.41 and 1.86 μM , respectively. The *in vitro* anticancer potentialities of PT-CS-NP were much better than those of sorafenib (4.13 and 7.55 μM) against the same cell lines, respectively. Values are given as the mean \pm SEM of triplicates. The obtained results indicate the promising enhancement in the anticancer effect because of chitosan nanoparticle encapsulation.

2.3.2. Safety and Selectivity Indices Calculation. To examine the safety of PT-CS-NP, CS, and PT and to investigate the selectivity of the examined candidates against cancer, the cytotoxic activity of PT-CS-NP, CS, and PT against the normal human W138 cell line was evaluated. The selectivity index of a compound is determined by dividing the IC_{50} against the normal cell line by IC_{50} against the cancer cell line.

As shown in Table 3 and Figure 8, PT-CS-NP CS was the safest candidate showing an extremely high IC_{50} value of 74.88 μM as well as excellent selectivity indices (SIs) against both MCF-7 and HCT 116 cell lines of 31.07 and 40.26, respectively.

2.4. Analysis. In order to examine the concentration as well as the release of PT, a novel differential pulse voltammetric analysis for PT was structured.

2.4.1. Mn_2O_3 Nanoparticles (NPs) Characterization. The preparation of Mn_2O_3 was chemically executed by

TABLE 2: *In vitro* antiproliferative activities of CS, PT, and PT-CS-NP against A549 and HCT 116 cell lines.

	MCF-7 IC_{50} (μM)	HCT 116 IC_{50} (μM)
PT-CS-NP	2.41	1.86
PT	18.17	7.95
CS	8.85	4.7
Sorafenib	4.13	7.55

precipitation tactic. SEM and TEM approaches were utilized for characterizing the samples. The outcomes displayed that the Mn_2O_3 form had a cubic pattern. The Mn_2O_3 crystals' average size was 80 nm according to the Scherrer formula in comparison with the value (106 nm) via the application of the Williamson–Hall technique.

The prepared nanostructure material's surface morphology characterization and average particle size were carried out by SEM and TEM, respectively. Figure 9(a) displays the Mn_2O_3 SEM image nanoparticles dispersed with a cubic-hexagonal form on the surface [39]. In addition, Figure 9(b) characterizes the Mn_2O_3 nanoparticles TEM image in a sphere-shaped form with an average size of 70 nm.

2.4.2. The Different Electrodes Morphologies. The electroactive area was calculated for each electrode by the Randles–Sevcik equation [40–41] utilizing $K_3Fe(CN)_6$ ($1.0 \times 10^{-3} M$) in 0.1 M KCl observed by CV at multiple scanning rates. Then, the efficient areas on the surface were computed to be 0.07 and 0.34 cm^2 for bare and Mn_2O_3 NPs/CPE 5% electrodes, respectively. The electrode geometrical surface was 0.057 cm^2 (for an id of 2 mm) which is extremely less than the active area of the surface. This authenticates that Mn_2O_3 NPs/CPE 5% has the highest operative surface area [42]. An enhancement in charge transporters and electrochemical efficiency indicated the large surface area.

2.4.3. PT Electrochemistry. The carbon paste component is a fundamental item that influences the intensity of the current, resistance, hydrophilicity, and voltammetry of the newly modified electrode reaction. For exploring the influence, PT's anodic oxidation on peak behavior ($1.0 \times 10^{-4} M$) for two electrodes in B–R buffer (pH 4) and a scanning rate of 100 mV s^{-1} was registered and evaluated by DPV (Figure 10(a)). The peak current of oxidation was recorded to be 5.34 μA for CPE, whereas, in the case of Mn_2O_3 NPs/CPE 5%, the peak current of oxidation augmented to 11.94 μA with fewer shifts in the potential positive direction. The rise in the peak current thanks to a large quantity of manganese metal and thus verified the augmentation of the conductivity of the oxide. It can be decided that the anodic oxidation of PT can be determined from all the findings realized above. PT was experiencing adsorption and diffusion at the modifying electrode, where the electrode-generated hydroxyl radicals attacked the two phenol groups and then oxidized by losing two hydrogen atoms, creating a keto-derivative form. Figure 10(b) demonstrates

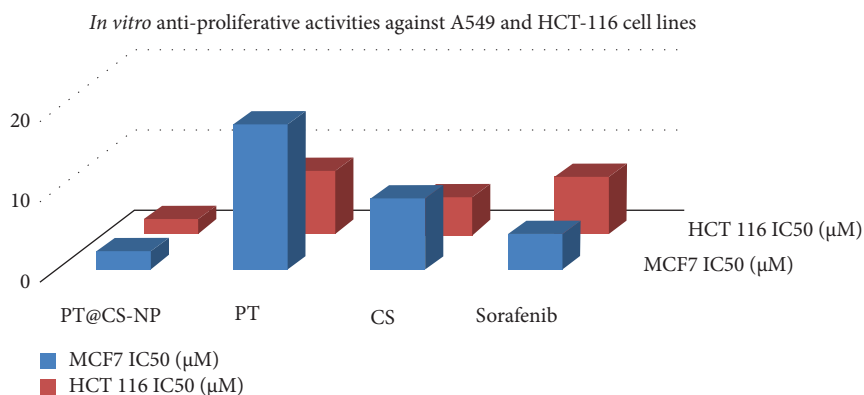


FIGURE 7: *In vitro* antiproliferative activities of CS, PT, and PT-CS-NP against A549 and HCT 116 cell lines.

TABLE 3: Antiproliferative activities against W138 cell lines and selectivity indices of PT-CS-NP, CS, and PT.

	W138 IC ₅₀ (µM)	SI (MCF 7)	SI (HCT 116)
PT-CS-NP	74.88	31.07	40.26
PT	102.19	5.62	12.85
CS	69.48	7.85	14.78
Sorafenib	71.96	16.66	9.88

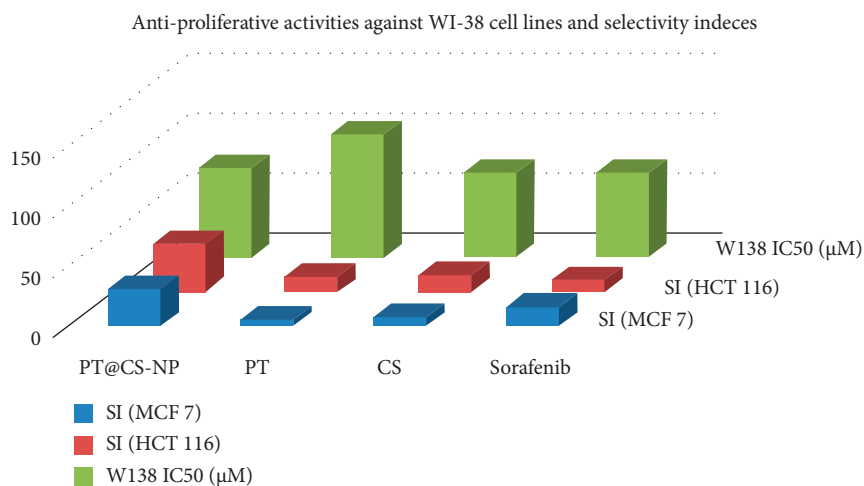


FIGURE 8: Antiproliferative activities against W138 cell lines and selectivity indices of PT-CS-NP, CS, and PT.

the schematic voltammetry response behavior of the electrodes.

2.4.4. Experimental Conditions Optimization

(1) *The pH Effect.* The pH ranged from 2 to 7 utilizing *B-R* buffer, which performs an essential part in examining PT's oxidation method at Mn₂O₃NPs/MCPE 5%. This was approved by a negative shifting in anodic peak oxidation with a rise in the PT solution's pH to confirm the participation of protons on the electrode, as revealed in Figure 11. It was found that pH 4.0 provided the maximum signals of electro-oxidation that had a full peak potential of about +0.53 V.

Concerning the pKa value of 6.95 (acidic pKa for phenolic groups), the bulk of PT molecules are in the cationic state at pH 4, leading to an electrostatic attraction between the anodic-activated Mn₂O₃NPs/CPE and PT molecules. At pH less than 4, the solution has protons in high concentration that blocks PT oxidation and diminishes the peak current of oxidation. On the other side, at pH higher than pH 4, the peak current of voltammetry was decreased. Consequently, pH 4.0 was selected for the consequent examinations.

Following the literature, the peak potential had several values via changing the solution's pH. For the modified electrode, an intense linear relationship was created between pH and potential (E_p) as described by the consequent equation:

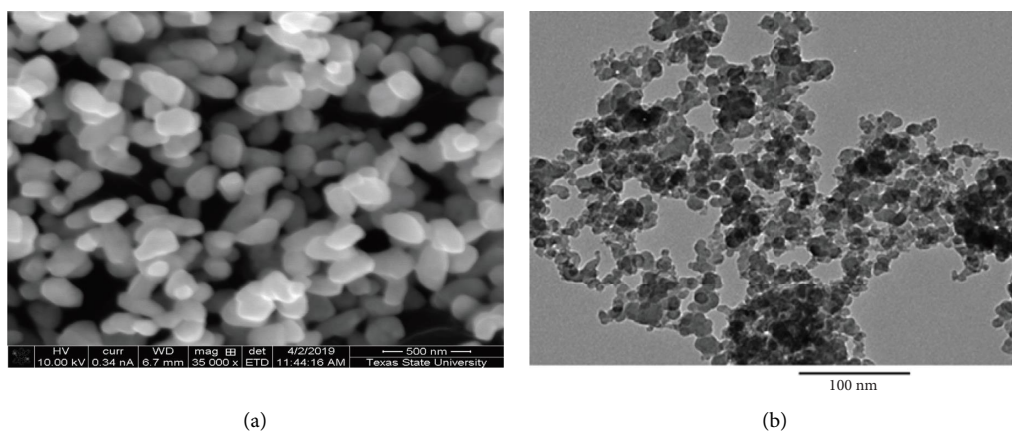
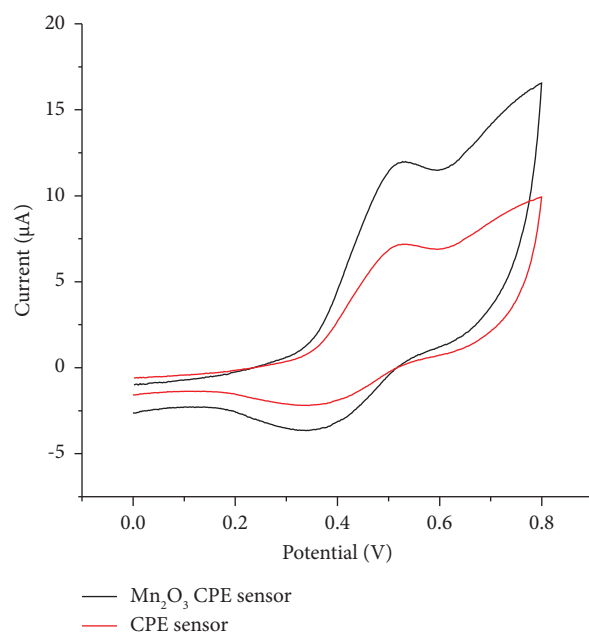
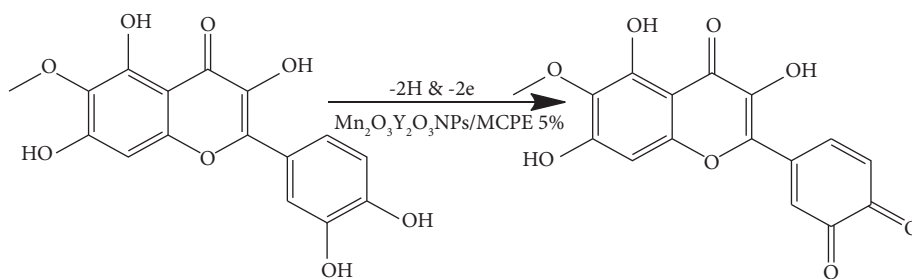


FIGURE 9: (a) SEM images of Mn₂O₃ and (b) TEM images of Mn₂O₃.



(a)



(b)

FIGURE 10: (a) Influence of different modified electrodes on the peak current of oxidation during PT (1.00 × 10⁻⁴ M) determination at a 100 mV s⁻¹ scanning rate and in B-R buffer (pH 4) and (b) schematic interaction in the CP electrode for PT molecules and Mn₂O₃NPs 5%.

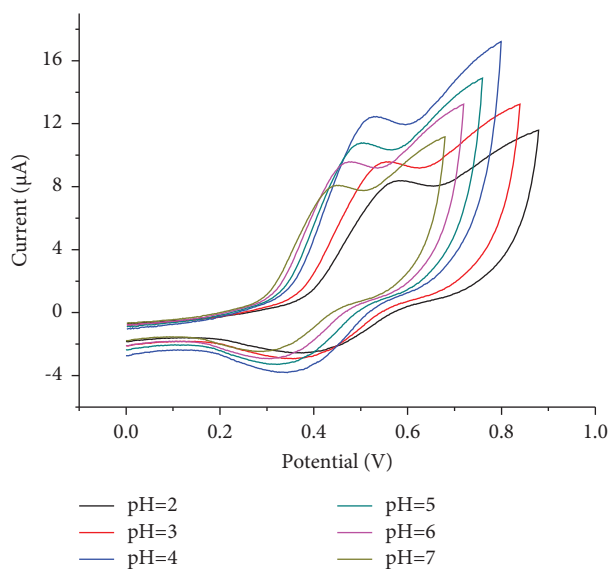


FIGURE 11: The effect of the oxidation peak potential for ($1.00 \times 10^{-4} M$) PLN at different pH on the created current using Mn_2O_3NPs/CPE 5% electrode.

$$E_p (V) = 0.705 - 0.053 \text{ pH } r = 0.996 \text{ for } \frac{Mn_2O_3NPs}{MCPE} 5\%. \quad (1)$$

The slope produced was Nernstian, which changes drastically with the Nernstian values ($60 \pm 11 \text{ mV/pH}$), signifying the same charge number (two protons and two electrons) on the surface of the modified electrode in PT electrochemical oxidation.

(2) *The Scanning Rate Effect.* The scanning rate had a vital part in identifying PLN's mechanism of oxidation at Mn_2O_3NPs/CPE 5% electrode by the registration of suitable oxidation peak currents' response at various registered scanning rates (20: 160 mV s^{-1}) by the CV ($1.00 \times 10^{-4} M$).

The peak current plots for oxidation (I_{pa}) versus the quadratic root for the scanning rates ($v^{1/2}$) were not linear along all concentration ranges, as revealed in Figure 12, which approves combined diffusion and adsorption in this range, and the correlative equation is as follows:

$$I_p (\mu A) = 0.0145 v^{1/2} (\text{mV s}^{-1}) + 0.108. \quad (2)$$

On the other side, via plotting the logarithmic values of peak currents for oxidation versus the logarithmic values of scanning rates, a linear intense relationship was achieved as demonstrated in the following equation:

$$\text{Log } I_p = 1.89 + 0.755 \text{ log } v. \quad (3)$$

The derived slope value (0.755) demonstrated that the actual electroactive species transfer mechanism was the adsorption and diffusion-controlled process.

For irreversible processes, Laviron's theory [40, 41] was implemented to determine the electron-transfer kinetics and number of electrons that were conveyed during PLN oxidation on the surface of the Mn_2O_3NPs/CPE 5% electrode.

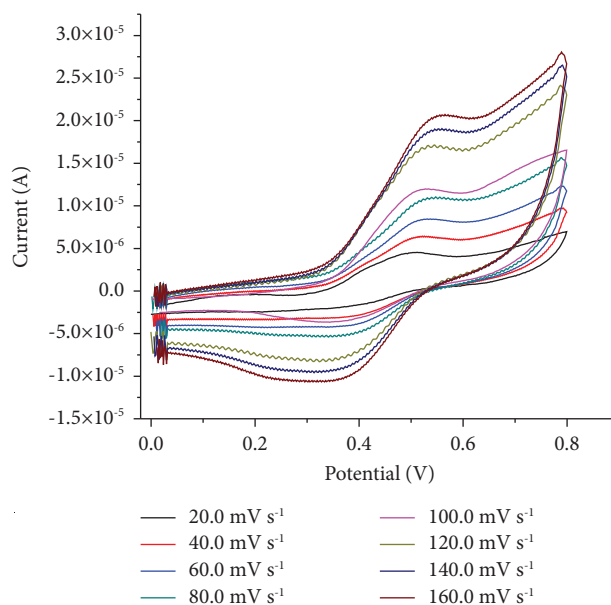


FIGURE 12: Cyclic voltammogram responses of PLN ($1.00 \times 10^{-4} M$) in *B-R* buffer (pH 4.0) at different scanning rates (20.0: 160.0 mVs^{-1}) utilizing Mn_2O_3NPs/CPE 5% electrode.

$$E = E^0 + \frac{2.303 RT}{\alpha n F} \left(\log \frac{RTK^0}{\alpha n F} \right) + \frac{2.303 RT}{\alpha n F} (\log v). \quad (4)$$

The derived slope for the predicted relationship between log scanning rate and applied potential was performed to compute αn , where n is the electron number and α is the coefficient of electron transfer contributed to the oxidation. The peak potential for oxidation (E_p) was as well reliant on the scanning rate, where the scanning rate increase led to a further positive potential shift.

$$E_p (V) = 0.5851 + 0.043 \text{ log } v \text{ mVs}^{-1} r = 0.997. \quad (5)$$

As stated by the previous equation, the slope was 0.043, and αn was computed to be 1.16. In general, the theoretical value of α was suggested to be 0.5 and then n was computed to be 2.3 (≈ 2), which was well-matched with the suggested PLN mechanism for oxidation where two electrons were implemented. In addition, the rate constant for charge transfer, k_s , for the anodic voltammetry reaction was computed to be around $2.04 \times 10^3 \text{ S}^{-1}$ by Laviron's theory [43–45].

2.4.5. Method Validation. The criteria and ideas for validation of the suggested method were executed in compliance with the ICH guidelines [46].

(1) *Linearity.* There was a significant direct correlation between PLN concentration and the resulting peak current, as demonstrated in Figure 13 and Table 4.

(2) *Limits for Detection and Quantification.* By using the following equations, LOD and LOQ were computed to be 3.4 nM and 9.0 nM, respectively:

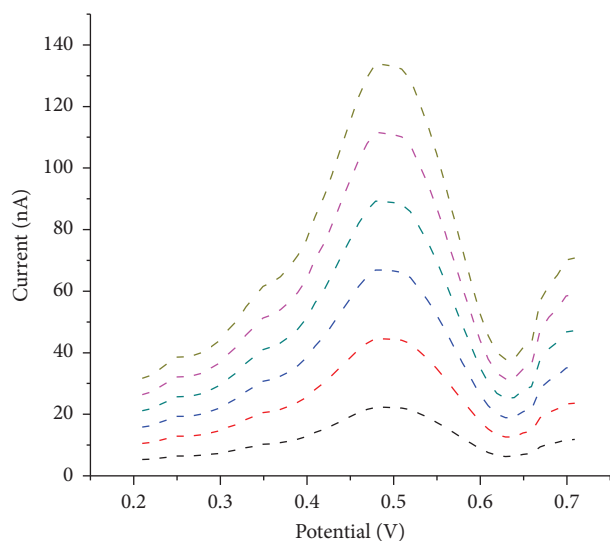


FIGURE 13: DPV voltammograms for different concentrations of PLN at $\text{Mn}_2\text{O}_3\text{NPs/CPE 5\%}$ electrode.

TABLE 4: Parameters of validation of the recommended voltammetric technique for PT determination.

Parameters	DPV method
Linearity (M)	10.0×10^{-9} : 10.0×10^{-5}
LOD (M)	3.4×10^{-9}
LOQ (M)	9.0×10^{-9}
Slope	0.194
Intercept	4.129
The correlation coefficient (r)	0.996
Accuracy Mean \pm RSD %	100.13 ± 0.895
Precision (RSD%)	
Repeatability	0.764
Intermediate precision	0.766

$\text{LOD} = 3.3 * \text{standard deviation/slope}$ and $\text{LOQ} = 10 * \text{standard deviation/slope}$.

(3) *Accuracy and Precision*. The accuracy of the proposed method for estimating PLN states how the metrics were close to their theoretical values and evaluated as % recovery, whereas precision states how the metrics were close to each other and evaluated as % relative standard deviation. The found outcomes are precise and accurate as introduced in Table 4.

(4) *Robustness*. Robustness evaluates the suggested method adaptability via minor premeditated variations in a specific factor while maintaining the other factors fixed, for instance, a minor change in the accumulation time ($20 \text{ s} \pm 2 \text{ s}$) or pH (4.0 ± 0.1). The responses were not influenced by the slight changes, confirming the method is robust.

3. Conclusion

The study presented herein describes the production of chitosan nanoparticles that have been encapsulated with patuletin (PT-CS-NP) using the ionic gelation method.

The encapsulation efficiency of PT-CS was initially estimated computationally and was later confirmed through various analytical techniques, including FT-IR, SEM, TEM, and TGA. Encouragingly, the results demonstrate that PT-CS-NP has a potent cytotoxic effect against cancer cells MCF-7 and HCT 116, with IC_{50} values of 2.41 and 1.86 μM , respectively. Notably, PT-CS-NP also exhibits high selectivity indices of 31.07 and 40.26 for the two cell types, respectively. Furthermore, the use of Mn_2O_3 and graphite at CPE enhances the electromagnetic properties and enables it to be used as a chemical sensor for detecting PT with high sensitivity, accuracy, and selectivity. These findings indicate that the proposed method can efficiently detect PT at low levels over a wide range with high precision and rapid response.

4. Experimental Setup

4.1. *Materials for PT-CS-NP Synthesis*. Chitosan, tripolyphosphate, glacial acetic acid, and dimethyl sulfoxide (DMSO) as well as other materials that have been included in the synthesis of PT-CS-NP are mentioned in the Supplementary materials.

4.2. *Preparation of PT-CS-NP*. The preparation of PT-CS-NP was done by the ionotropic gelation method that is discussed extensively in the Supplementary materials.

4.3. *Characterization of PT-CS-NP*. Characterization procedures of the produced PT-CS-NP nanoparticles have been performed by four methods (FT-IR, TGA, SEM, and TEM) which are discussed extensively in the Supplementary materials.

4.4. *In Vitro Cytotoxicity*. In vitro cytotoxicity procedure against cancer (MCF-7 and HCT 116) and normal (W138) cells was done by MTS assay as discussed extensively in the Supplementary materials.

4.5. *Apparatus and Reagents*. Apparatus and reagents used for chemicals of analysis are mentioned in the Supplementary materials.

4.6. *Standard Solutions*. The preparation and use of standard solutions are discussed extensively in the Supplementary materials.

4.7. *Electrodes Construction*. Samples preparation for Mn_2O_3 , bare CPE, and modified CPEs fabrications are discussed extensively in the Supplementary materials.

4.8. *Measurements of Electrochemistry*. The electrochemical action of PT by voltammetry of the square wave and calibration curve procedure are discussed extensively in the Supplementary materials.

Data Availability

All data regarding this research are inclosed in the manuscript and in the supporting materials.

Conflicts of Interest

The authors declare that they have no conflicts of interest.

Acknowledgments

This research was funded by Princess Nourah bint Abdulrahman University Researchers Supporting Project number (PNURSP2023R142), Princess Nourah bint Abdulrahman University, Riyadh, Saudi Arabia. The authors extend their appreciation to the Research Center at AlMaarefa University for funding this work.

Supplementary Materials

Supplementary materials contain an extensive discussion and full methodology of the following: materials, preparation, characterization for PT-CS-N, *in vitro* anticancer and safety assays, apparatus, reagents, electrodes construction, and measurements of electrochemistry studies. (*Supplementary Materials*)

References

- [1] Who Cancer, "Fact sheet," 2022, <https://www.who.int/news-room/fact-sheets/detail/cancer>.
- [2] W. Iarc, "Colorectal cancer awareness month," 2021, <https://www.iarc.who.int/featured-news/ccam2021/>.
- [3] A. M. Metwaly, M. M. Ghoneim, I. H. Eissa et al., "Traditional ancient Egyptian medicine: a review," *Saudi Journal of Biological Sciences*, vol. 28, no. 10, pp. 5823–5832, 2021.
- [4] X. Han, Y. Yang, A. M. Metwaly, Y. Xue, Y. Shi, and D. Dou, "The Chinese herbal formulae (Yitangkang) exerts an anti-diabetic effect through the regulation of substance metabolism and energy metabolism in type 2 diabetic rats," *Journal of Ethnopharmacology*, vol. 239, Article ID 111942, 2019.
- [5] A. M. Metwaly, Z. Lianlian, H. Luqi, and D. J. M. Deqiang, "Black ginseng and its saponins: preparation, phytochemistry and pharmacological effects," *Molecules*, vol. 24, no. 10, p. 1856, 2019.
- [6] P. S. Rao and T. Seshadri, "The colouring matter of the flowers of *Tagetes patula*: isolation of a new flavonol, patuletin and its constitution," *Proceedings of the Indian Academy of Sciences-Section A*, Springer, Berlin, Germany, 1941.
- [7] M. A. Abdel-Wahhab, A. Said, and A. Huefner, "NMR and radical scavenging activities of patuletin from *Urtica urens*. Against aflatoxin B1," *Pharmaceutical Biology*, vol. 43, no. 6, pp. 515–525, 2005.
- [8] E. Bate-Smith and J. Harborne, "Quercetagenin and patuletin in *Eriocaulon*," *Phytochemistry*, vol. 8, no. 6, pp. 1035–1037, 1969.
- [9] Y.-M. Wang, X.-K. Ran, M. Riaz et al., "Chemical constituents of stems and leaves of *Tagetes patula* L. and its fingerprint," *Molecules*, vol. 24, no. 21, p. 3911, 2019.
- [10] M. Azhar, A. D. Farooq, S. Haque, S. Bano, L. Zaheer, and S. J. T. J. O. B. Faizi, "Cytotoxic and genotoxic action of *Tagetes patula* flower methanol extract and patuletin using the Allium test," *Allium test*, vol. 43, no. 5, pp. 326–339, 2019.
- [11] H. Woerdenbag, I. Merfort, T. Schmidt et al., "Decreased helenalin-induced cytotoxicity by flavonoids from *Arnica* as studied in a human lung carcinoma cell line," *Phytomedicine*, vol. 2, no. 2, pp. 127–132, 1995.
- [12] J. J. Alvarado-Sansininea, L. Sánchez-Sánchez, H. López-Muñoz et al., "Quercetagenin and patuletin: antiproliferative, necrotic and apoptotic activity in tumor cell lines," *Molecules*, vol. 23, no. 10, p. 2579, 2018.
- [13] M. Kashif, S. Bano, S. Naqvi et al., "Cytotoxic and antioxidant properties of phenolic compounds from *Tagetes patula* flower," *Pharmaceutical Biology*, vol. 53, no. 5, pp. 672–681, 2015.
- [14] H. J. Woerdenbag, I. Merfort, C. Paßreiter et al., "Cytotoxicity of flavonoids and sesquiterpene lactones from *Arnica* species against the GLC4 and the COLO 320 cell lines," *Planta Medica*, vol. 60, no. 5, pp. 434–437, 1994.
- [15] A. Jabeen, M. A. Mesaik, S. U. Simjee, S. Bano, S. Bano, and S. Faizi, "Anti-TNF- α and anti-arthritis effect of patuletin: a rare flavonoid from *Tagetes patula*," *International Immunopharmacology*, vol. 36, pp. 232–240, 2016.
- [16] M. Zarei, S. Mohammadi, and A. Komaki, "Antinociceptive activity of *Inula britannica* L. and patuletin: in vivo and possible mechanisms studies," *Journal of Ethnopharmacology*, vol. 219, pp. 351–358, 2018.
- [17] S. Faizi, H. Siddiqi, S. Bano et al., "Antibacterial and antifungal activities of different parts of *Tagetes patula*: preparation of patuletin derivatives," *Pharmaceutical Biology*, vol. 46, no. 5, pp. 309–320, 2008.
- [18] M. L. Tereschuk, M. V. Riera, G. R. Castro, and L. R. J. J. O. E. Abdala, "Antimicrobial activity of flavonoids from leaves of *Tagetes minuta*," *Journal of Ethnopharmacology*, vol. 56, no. 3, pp. 227–232, 1997.
- [19] L. Liu, S. Luo, M. Yu et al., "Chemical constituents of *tagetes patula* and their neuroprotecting action," *Natural Product Communications*, vol. 15, no. 11, Article ID 1934578X2097450, 2020.
- [20] A. Sosnik and R. Augustine, "Challenges in oral drug delivery of antiretrovirals and the innovative strategies to overcome them," *Advanced Drug Delivery Reviews*, vol. 103, pp. 105–120, 2016.
- [21] Z. Muldakhmetov, S. Fazylov, O. Nurkenov et al., "Combined computational and experimental studies of anabasine encapsulation by beta-cyclodextrin," *Plants*, vol. 11, no. 17, p. 2283, 2022.
- [22] A. Iskineyeva, S. Fazylov, R. Bakirova et al., "Combined in silico and experimental investigations of resveratrol encapsulation by beta-cyclodextrin," *Plants*, vol. 11, no. 13, p. 1678, 2022.
- [23] G. Kravanja, M. Primožič, Ž. Knez, and M. Leitgeb, "Chitosan-based (Nano) materials for novel biomedical applications," *Molecules*, vol. 24, no. 10, p. 1960, 2019.
- [24] S. G. Kou, L. M. Peters, and M. R. J. I. J. O. B. M. Mucalo, "Chitosan: a review of sources and preparation methods," *International Journal of Biological Macromolecules*, vol. 169, pp. 85–94, 2021.
- [25] M. Soltani, A. Etminan, A. Rahmati, M. Behjati Moghadam, G. Ghaderi Segonbad, and M. J. M. T. Homayouni Tabrizi, "Incorporation of *Boswellia sacra* essential oil into chitosan/TPP nanoparticles towards improved therapeutic efficiency," *Materials Technology*, vol. 37, no. 11, pp. 1703–1715, 2022.
- [26] E. Yousefian Rad, M. Homayouni Tabrizi, P. Ardalan et al., "Citrus lemon essential oil nanoemulsion (CLEO-NE), a safe cell-dependent apoptosis inducer in human A549 lung cancer

- cells with anti-angiogenic activity,” *Journal of Microencapsulation*, vol. 37, no. 5, pp. 394–402, 2020.
- [27] J. Liu, Y. Xu, S. Liu, S. Yu, Z. Yu, and S. S. J. B. Low, “Application and progress of chemometrics in voltammetric biosensing,” *Biosensors*, vol. 12, no. 7, p. 494, 2022.
- [28] A. M. Metwaly, E. B. Elkaeed, B. A. Alsouk, A. M. Saleh, A. E. Mostafa, and I. H. J. P. Eissa, “The computational preventive potential of the rare flavonoid, patuletin, isolated from *Tagetes patula*, against SARS-CoV-2,” *Plants*, vol. 11, no. 14, p. 1886, 2022.
- [29] A. Elzatahry and M. S. M. Eldin, “Preparation and characterization of metronidazole-loaded chitosan nanoparticles for drug delivery application,” *Polymers for Advanced Technologies*, vol. 19, no. 12, pp. 1787–1791, 2008.
- [30] M. Moustafa, M. Abu-Saied, T. H. Taha et al., “New blends of acrylamide/chitosan and potato peel waste as improved water absorbing polymers for diaper applications,” *Polymers and Polymer Composites*, vol. 30, Article ID 096739112210775, 2022.
- [31] A. M. dos Santos, S. G. Carvalho, L. M. B. Ferreira, M. Chorilli, and M. P. D. Gremião, “Understanding the role of electrostatic interactions on the association of 5-fluorouracil to chitosan-TPP nanoparticles,” *Colloids and Surfaces A: Physicochemical and Engineering Aspects*, vol. 640, Article ID 128417, 2022.
- [32] K. V. Jardim, J. L. N. Siqueira, S. N. Bão, and A. L. Parize, “In vitro cytotoxic and antioxidant evaluation of quercetin loaded in ionic cross-linked chitosan nanoparticles,” *Journal of Drug Delivery Science and Technology*, vol. 74, Article ID 103561, 2022.
- [33] M. Ateeq, M. R. Shah, N. U. Ain et al., “Green synthesis and molecular recognition ability of patuletin coated gold nanoparticles,” *Biosensors and Bioelectronics*, vol. 63, pp. 499–505, 2015.
- [34] A. G. Raja, K. A. S. Arasu, R. Rajaram, and Synthesis, “Characterization and application of chitosan-TPP-ZnO nanocomposite for efficient treatment of effluent containing sulphur dye,” *Materials Today: Proceedings*, vol. 18, 2022.
- [35] S. Soleymanfallah, Z. Khoshkhoo, S. E. Hosseini, and M. H. Azizi, “Preparation, physical properties, and evaluation of antioxidant capacity of aqueous grape extract loaded in chitosan-TPP nanoparticles,” *Food Science and Nutrition*, vol. 10, no. 10, pp. 3272–3281, 2022.
- [36] R. Nunes, A. S. Serra, A. Simaite, and Â. Sousa, “Modulation of chitosan-TPP nanoparticle properties for plasmid DNA vaccines delivery,” *Polymers*, vol. 14, no. 7, p. 1443, 2022.
- [37] M. Moustafa, M. A. Abu-Saied, T. H. Taha et al., “Preparation and characterization of super-absorbing gel formulated from κ -carrageenan-potato peel starch blended polymers,” *Polymers*, vol. 13, no. 24, p. 4308, 2021.
- [38] J. Li, H. Wu, K. Jiang, Y. Liu, L. Yang, and H. J. Park, “Alginate calcium microbeads containing chitosan nanoparticles for controlled insulin release,” *Applied Biochemistry and Biotechnology*, vol. 193, no. 2, pp. 463–478, 2021.
- [39] A. Kruk, A. Wajler, M. Bobruk et al., “Preparation of yttria powders co-doped with Nd³⁺, and La³⁺ using EDTA gel processes for application in transparent ceramics,” *Journal of the European Ceramic Society*, vol. 37, no. 13, pp. 4129–4140, 2017.
- [40] A. M. Abdel-Raoof, M. A. El-Shal, R. A. Said, M. H. Abostate, S. Morshedy, and M. S. J. J. T. E. S. Emara, “Versatile sensor modified with gold nanoparticles carbon paste electrode for anodic stripping determination of brexpiprazole: a voltammetric study,” *Journal of the Electrochemical Society*, vol. 166, no. 12, pp. B948–B955, 2019.
- [41] S. A. Atty, H. E. Zaazaa, F. A. Morsy, D. M. Naguib, and G. A. J. J. T. E. S. Sedik, “Nano green voltammetric determination of imidocarb dipropionate and its residues in bovine meat, milk and urine samples,” *Journal of the Electrochemical Society*, vol. 167, no. 4, Article ID 047510, 2020.
- [42] T. Tamiji and A. J. J. O. T. T. I. O. C. E. Nezamzadeh-Ejehieh, “Electrocatalytic behavior of AgBr NPs as modifier of carbon paste electrode in the presence of methanol and ethanol in aqueous solution: a kinetic study,” *Journal of the Taiwan Institute of Chemical Engineers*, vol. 104, pp. 130–138, 2019.
- [43] M. Nosuhi and A. J. I. Nezamzadeh-Ejehieh, “A sensitive and simple modified zeolitic carbon paste electrode for indirect voltammetric determination of nitrate,” *Ionics*, vol. 24, no. 7, pp. 2135–2145, 2018.
- [44] N. Ghasemi and A. J. N. J. O. C. Nezamzadeh-Ejehieh, “Study of the interactions of influencing parameters on electrocatalytic determination of dopamine by a carbon paste electrode based on Fe (ii)-clinoptilolite nanoparticles,” *New Journal of Chemistry*, vol. 42, no. 1, pp. 520–527, 2018.
- [45] M. S. Tohidi and A. J. I. J. O. H. E. Nezamzadeh-Ejehieh, “A simple, cheap and effective methanol electrocatalyst based of Mn (II)-exchanged clinoptilolite nanoparticles,” *International Journal of Hydrogen Energy*, vol. 41, no. 21, pp. 8881–8892, 2016.
- [46] I. H. T. Guideline, “Validation of analytical procedures: text and methodology,” *Q2 (R1)*, vol. 1, no. 20, p. 5, 2005.
- [47] S. Sharafzadeh and A. Nezamzadeh-Ejehieh, “Using of anionic adsorption property of a surfactant modified clinoptilolite nano-particles in modification of carbon paste electrode as effective ingredient for determination of anionic ascorbic acid species in presence of cationic dopamine species,” *Electrochimica Acta*, vol. 184, pp. 371–380, 2015.